

NUMERICAL EVIDENCE FOR SINGULARITY FORMATION IN DEFOCUSING FRACTIONAL NLS IN ONE SPACE DIMENSION

CHRISTIAN KLEIN AND CHRISTOF SPARBER

ABSTRACT. We consider nonlinear dispersive equations of Schrödinger-type involving fractional powers $0 < s \leq 1$ of the Laplacian and a defocusing power-law nonlinearity. We conduct numerical simulations in the case of small, energy supercritical s and provide evidence for a novel type of highly oscillatory singularity within the solution.

1. INTRODUCTION

In this work, we shall be interested in fractional nonlinear Schrödinger equations (fNLS) of the form

$$(1.1) \quad i\partial_t u = (-\Delta)^s u + |u|^{2p} u, \quad u|_{t=0} = u_0,$$

where $(t, x) \in \mathbb{R} \times \mathbb{R}^d$ (although we shall mainly study the case $d = 1$), $p \in \mathbb{N}$ a nonlinear parameter, and $0 < s \leq 1$, the *fractional power* of the Laplacian. The latter is defined as a Fourier-multiplier with symbol $\lambda(\xi) = |\xi|^{2s}$, i.e.

$$(-\Delta)^s u = \mathcal{F}^{-1}(|\xi|^{2s} \hat{u}),$$

where $\hat{u} \equiv \mathcal{F}u$ denotes the Fourier transform of u .

Linear equations of the form (1.1) were introduced by Laskin in an attempt to generalize the Feynman path integral of classical quantum mechanics to Levy processes [30]. Their nonlinear counterpart appears in various applications, for example in the description of water waves [20], or in the continuum limit of certain long-range lattice-models [21]. Due to their strong resemblances to the well-studied classical NLS (obtained for $s = 1$), they are an active field of mathematical research in which one tries to extend previous results to a fractional, and thus nonlocal setting, see, e.g., [3, 9, 17, 25, 28] and the references therein.

Let us recall that solutions to (1.1) formally satisfy the conservation laws of *mass*

$$(1.2) \quad M(u) = \int_{\mathbb{R}^d} |u|^2 dx,$$

and *energy*

$$(1.3) \quad E(u) = \frac{1}{2} \int_{\mathbb{R}^d} |(-\Delta)^{s/2} u|^2 dx + \frac{1}{2p+2} \int_{\mathbb{R}^d} |u|^{2p+2} dx.$$

A natural energy space for solutions u is therefore $H^s(\mathbb{R}^d)$, assuming that $p \in \mathbb{N}$ is small enough to allow for the Sobolev-embedding $H^s(\mathbb{R}^d) \hookrightarrow L^{2p+2}(\mathbb{R}^d)$. One should note that, due to our choice of sign in front of the nonlinearity, the energy is the sum of two non-negative terms and hence, we are in what is called the *defocusing regime*.

Date: February 12, 2025.

2000 Mathematics Subject Classification. 65M70, 65L05, 35Q55.

Key words and phrases. Nonlinear Schrödinger equations, fractional Laplacian, Fourier spectral method, small dispersion, finite time blow-up.

This publication is supported by the MPS Simons foundation through award no. 851720, the ANR project ANR-17-EURE-0002 EIPHI, and the ANR project ISAAC-ANR-23-CE40-0015-01.

Equation (1.1) also enjoys the scaling invariance

$$u(t, x) \mapsto \frac{1}{\lambda^{s/p}} u\left(\frac{t}{\lambda^{2s}}, \frac{x}{\lambda}\right),$$

which is seen to leave the homogenous Sobolev-norm $\dot{H}^\sigma(\mathbb{R}^d)$ invariant, provided $\sigma = \sigma_c$, where

$$\sigma_c = \left(\frac{d}{2} - \frac{s}{p}\right).$$

One consequently refers to the Cauchy problem (1.1) with $u_0 \in H^\sigma$ and $\sigma \geq \sigma_c$ as H^σ (sub-)critical, whereas the case when $\sigma < \sigma_c$ is called H^σ supercritical. To link this notion of criticality to the energy space, one compares σ_c with the fractional power $s \in (0, 1]$, appearing as a parameter in (1.1). Doing so implies that solutions $u(t, \cdot) \in H^s(\mathbb{R}^d)$ are *energy (sub-)critical* if $s \geq s_*$, where

$$(1.4) \quad s_*(d, p) = \frac{d}{2} \left(\frac{p}{p+1}\right),$$

while the *energy supercritical* regime corresponds to $s < s_*$. The former regime is rather well understood and the (local) well-posedness theory for (1.1) in critical and sub-critical cases is, by now, broadly developed, cf. [9, 17, 28].

A systematic numerical study of equations of the form (1.1) has first been done by the authors together with P. Markowich in [25]. Here, we shall revisit these numerical simulations and expand on a particular case which has only been hinted at in [25]. Namely, the possibility of a novel type of *singularity formation in the defocusing case* with sufficiently *small (fractional) dispersion*.

This phenomenon needs to be clearly distinguished from the possibility of finite-time blow-up appearing in the case of *focusing* nonlinearities. In the focusing case, the kinetic and nonlinear potential energies in (1.3) have opposite signs, which allows for the existence of solitary waves (not present in the defocusing case). For $s = 1$, it is well known that $E(u_0) < 0$ is a sufficient condition for finite-time blow-up of (strong) solutions $u \in C([0, T]; H^s(\mathbb{R}^d))$, see, e.g., [34]. The blow-up is found to be self-similar with profiles given by the corresponding solitary wave solution. This basic picture has been successfully transferred to the case of fractional equations with $s \neq 1$, cf. [3] and the references given therein.

In contrast to the focusing situation it has long been believed that defocusing equations do not suffer from any singularity formation, cf. [4, 10]. Indeed, it has recently been proved in [18, 19] that defocusing one-dimensional dispersive equations with *small* (and not necessarily localized) initial data have *global dispersive solutions*. Nevertheless, a first rigorous proof of finite-time blow-up in *energy supercritical defocusing NLS* ($s = 1$) has been obtained by Merle et al. in their seminal paper [33]. In their work, blow-up of radial solutions u is achieved by compression in the associated (classical) hydrodynamical flow of ρ and $v = \nabla\varphi$, which is associated to u via the Madelung transform $u = \sqrt{\rho}e^{i\varphi}$. By using a self-similar ansatz for both ρ and v , and relying on analogous results for the compressible Euler equations [31, 32], Merle et al. are able to prove the appearance of an oscillatory singularity with universal profile

$$u(t, x) \underset{|x| \rightarrow 0}{\sim} \frac{c_1}{|x|^{(r-1)/p}} \exp\left(i \frac{c_2}{|x|^{r-2}}\right).$$

Here, $r = r(p, d) > 2$ denotes the blow-up speed and $c_1, c_2 > 0$ are constants depending on p, d and the initial data. Note that, both, the amplitude and the phase of u become singular at the origin.

The proof of this result requires the authors of [33] to work in dimensions $d \geq 5$ and to choose particular pairs of parameters (d, p) . Even though it is believed that the blow-up also exists for other choices of such pairs, it is unclear at this point what

the range of suitable p is for any given dimension $d \in \mathbb{N}$. Very recently, an extension to the case of *non-radial blow-up* scenarios in both \mathbb{R}^d and \mathbb{T}^d was provided in [6] for the particular choice $(d, p) = (8, 1)$. A drawback of all of these works is that the class of initial data for which the blow-up is proven is *not* explicitly specified (one only knows that there exists a finite co-dimensional manifold of smooth initial conditions). In particular, there is no clear threshold for u_0 identified beyond which blow-up will occur. This is a profound obstacle for possible numerical simulations.

In the present paper, we shall demonstrate numerical evidence for highly oscillatory singularity formation *already in* $d = 1$, provided the fractional (dispersive) power $s < s_*$ is sufficiently small. To this end, we shall choose several kinds of explicit initial data which are smooth, rapidly decaying and of size $\mathcal{O}(1)$ in $L^\infty \cap L^2$, cf. Section 4 for details. From now on, we shall restrict ourselves to the situation in $d = 1$ and impose

$$u_0 \in \mathcal{S}(\mathbb{R}) \subset \bigcap_{\sigma \in \mathbb{R}} H^\sigma(\mathbb{R}).$$

Assuming for the moment, that there exists a unique local in-time solution

$$u \in C([0, T]; H^s(\mathbb{R})) \text{ up to some } T > 0,$$

we realize that the critical Sobolev-index $s = \frac{1}{2}$ is significant in this context. Indeed, any solution $u(t, \cdot) \in H^s(\mathbb{R})$ to (1.1) with $s > \frac{1}{2}$, automatically satisfies $s > s_*$ for all $p \in \mathbb{N}$ and hence, we are in an energy subcritical regime. In addition, the conservation laws of mass (1.2) and energy (1.3) yield the uniform bound

$$\|u(t, \cdot)\|_{H^s(\mathbb{R})}^2 \leq M(u_0) + 2E(u_0), \quad \forall t \in [0, T],$$

which implies $T = +\infty$, i.e. global existence holds. In addition, by Sobolev imbedding, we know that if $s > \frac{1}{2}$: $H^s(\mathbb{R}) \hookrightarrow L^q(\mathbb{R})$ for all $q \geq 2$, and thus all L^q -norms of $u(t, \cdot)$ are uniformly bounded in this case (in particular, this holds for the nonlinear potential energy).

The situation with $s < \frac{1}{2}$ is more complicated: in view of the Gagliardo-Nirenberg inequality, we know that for any $\theta \in (0, 1)$, there exists a constant $C = C(M(u_0), E(u_0)) > 0$, such that

$$\|u\|_{L^q(\mathbb{R})} \lesssim \|u\|_{L^2(\mathbb{R})}^{1-\theta} \|u\|_{H^s(\mathbb{R})}^\theta \lesssim C,$$

provided $q = \frac{2}{1-2s} > 2$ with $s < \frac{1}{2}$. Given a particular choice of $s < \frac{1}{2}$ this yields a uniform bound on some higher order L^q -norm of the solution $u(t, \cdot)$, and thus for the full range $q \in [2, \frac{2}{1-2s}]$. (Here, we implicitly assume that the nonlinear power $p \in \mathbb{N}$ is such that $q = 2p + 2$ is within this admissible range, in order to guarantee that the nonlinear potential energy of u is well-defined.) Clearly, this higher order L^q -bound deteriorates as $s \rightarrow 0$ and eventually only yields the obvious bound on the L^2 -norm (or mass) of u . For small enough $s < \frac{1}{2}$ this consequently leaves open the possibility that the solution might develop a singularity in some higher L^q -norm where $2 < q \leq \infty$.

Let us note that $s < \frac{1}{2}$ does not necessarily correspond to an energy supercritical regime. Indeed, the smallest energy critical index in $d = 1$ is found to be $s_* = \frac{1}{4}$, obtained in the case of a cubic nonlinearity (where $p = 1$). More generally, we have the following range of critical indices

$$s_* = \frac{p}{2p+2} \in \left[\frac{1}{4}, \frac{1}{2} \right) \quad \text{in } d = 1.$$

This paper is now organized as follows: in Section 2 we introduce a semiclassical rescaling for fNLS and review the numerical methods deployed in our simulations. In Section 3 we discuss the linear fractional Schrödinger equation and some of its basic dynamical properties. Numerical simulations for various initial data in

the energy (sub-)critical regime are presented in Section 4. Finally, in Section 5 we shall provide numerical evidence for a singularity formation in various energy supercritical cases. In the appendix, we collect some remarks on the comparison of our numerical scheme with other numerical methods.

2. SEMICLASSICAL RESCALING AND NUMERICAL METHODS

2.1. Semiclassical rescaling. Recall that the blow-up phenomenon in [33] is given by a highly oscillatory singularity obtained from the underlying classical hydrodynamical flow. Motivated by these ideas, we shall consider (1.1) in a *semi-classical regime* which imprints high-frequency oscillations onto the solution.

To this end, let $\varepsilon \sim \hbar \ll 1$ be a small (dimensionless) *semi-classical parameter*, and consider slowly varying initial data of the form

$$u_0(x) = v(\varepsilon x),$$

where $v \in \mathcal{S}(\mathbb{R})$ is some given ε -independent profile of size $\mathcal{O}(1)$. As $\varepsilon \rightarrow 0$ the initial data approach the constant value $v(0)$. Hence, in order to see nontrivial effects within the solution, we will need to consider macroscopic length- and time-scales of order $\mathcal{O}(1/\varepsilon)$. As in [25] we rescale $x \mapsto \tilde{x} = \varepsilon x$, $t \mapsto \tilde{t} = \varepsilon t$, and denote the new unknown by

$$\tilde{u}(\tilde{t}, \tilde{x}) = u\left(\frac{\tilde{t}}{\varepsilon}, \frac{\tilde{x}}{\varepsilon}\right).$$

The latter solves a semi-classically scaled equation, where we discard the $\tilde{}$ again, for simplicity:

$$(2.1) \quad i\varepsilon \partial_t u = (-\varepsilon^2 \Delta)^s u + |u|^{2p} u, \quad u|_{t=0} = v(x),$$

At least for short times $0 < |t| < t_0$, we expect the solution to exhibit a highly oscillatory behavior of the form

$$(2.2) \quad u(t, x) \underset{\varepsilon \rightarrow 0}{\sim} a(t, x) e^{i\varphi(t, x)/\varepsilon},$$

where φ is some real-valued phase and a denotes a slowly varying amplitude.

Remark 2.1. For $s = 1$ it is well known that an ansatz of the form (2.2) allows one to study the semi-classical asymptotics of u as $\varepsilon \rightarrow 0$ via an Euler-type system obtained for the density $\rho = |a|^2$ and the velocity $v = \nabla \varphi$. The latter is known to be equivalent to the original Schrödinger equation, cf. [7]. In the case $s \neq 1$ no such equivalent formulation (or Madelung transform) is known at this point.

A particular situation appears in a regime with very small $s \ll 1$, which can be considered as a *small dispersion limit* for (2.1). Indeed, we see that (at least formally)

$$(-\varepsilon^2 \Delta)^s u \rightarrow \mathbf{1}u, \quad \text{as } s \rightarrow 0,$$

resulting in the following limiting equation

$$(2.3) \quad i\varepsilon \partial_t u_{\text{lim}} = (1 + |u_{\text{lim}}|^{2p}) u_{\text{lim}}, \quad u_{\text{lim}}|_{t=0} = v(x).$$

The latter is *non-dispersive* and its solution is explicitly given by

$$u_{\text{lim}}(t, x) = v(x) e^{-it(1+|v(x)|^{2p})/\varepsilon}.$$

This implies that the particle (or energy) density $|u_{\text{lim}}(t, x)|^2 = |v(x)|^2$ for all $t \in \mathbb{R}$ and is hence, ε -independent, while the solution itself is seen to exhibit (nonlinear) oscillation with frequency $\nu = \mathcal{O}(\frac{1}{\varepsilon})$.

Remark 2.2. In our numerical simulations below, we shall typically choose $\varepsilon = 0.1$. This allows us to accurately compute up to times of order $T \simeq 20$.

2.2. Numerical method for computing the time-evolution. To solve equation (2.1) numerically, we shall use a Fourier-spectral method similar to the one in [25]. This choice is motivated by the highly oscillatory nature of our problem with steep gradients and thus the need for very high numerical resolution. We refer to [26] for other possible approaches to numerically simulate fractional derivatives in less oscillatory situations.

To be more precise, we shall construct the numerical solution to (2.1) as

$$u(t, x) = (\mathcal{F}^{-1}\hat{u})(t, x),$$

where \hat{u} solves

$$(2.4) \quad i\varepsilon\partial_t\hat{u} = \varepsilon^{2s}|\xi|^{2s}\hat{u} + \mathcal{F}(|u|^2u), \quad \hat{u}|_{t=0} = \hat{v}(\xi).$$

We thereby consider $x \in [-L\pi, L\pi]$ with $L \gg 1$, and impose *periodic boundary conditions* to approximate $\hat{u}(\cdot, \xi) \approx \hat{u}(\cdot, k)$, i.e. the discrete Fourier-transform of $u(\cdot, x)$ with frequency-variable $k \in \frac{1}{2L}\mathbb{Z}$ (by a slight abuse of notation, we shall denote both the Fourier transform and its discrete version by the same symbol).

The function $\hat{u}(\cdot, k)$ can be conveniently computed using the Fast Fourier transform (FFT). We thereby apply the standard discretization for the FFT, using

$$x_n = \left(-\pi + \frac{2n\pi}{N}\right)L, \quad n = 1, \dots, N \in \mathbb{N},$$

with the corresponding discrete Fourier variable

$$k = \frac{1}{L} \left(-\frac{N}{2} + 1, \dots, \frac{N}{2}\right) \in \frac{1}{2L}\mathbb{Z}.$$

For functions $u(\cdot, x)$ that are analytic in $x \in [-L\pi, L\pi]$ within numerical precision (here, roughly 10^{-16}), it is well known that the numerical error decreases exponentially with N , see [36]. However, it was shown in [26, 27] that this exponential decrease in N cannot be expected to hold for fractional powers $s \notin \mathbb{N}$, since the Fourier-symbol $|k|^{2s}$ is no longer regular. Indeed, a Paley-Wiener argument implies that the inverse Fourier transform of $|k|^{2s}\hat{u}(\cdot, k)$ is not rapidly decreasing, even if $\hat{u}(\cdot, k)$ is in the class of Schwartz functions w.r.t. k . In turn this means that machine precision *cannot* be reached for non-integer $s \in (0, 1]$, see [27]. Indeed, in all of our simulations the numerical error remains of the order of 10^{-5} , even when using a very high spatial resolution. This (relatively large) numerical error is nevertheless acceptable for our purposes. In addition, the use of Fourier-methods allows us to implement a numerical algorithm for singularity tracing in the frequency domain, see Section 2.3 below.

The FFT discretization of (2.4) leads to an N -dimensional system of ordinary differential equations which for $s \simeq 1$ are *stiff* (meaning that explicit methods are usually inefficient in view of the required stability conditions). However, since the stiff terms are in the diagonal part of the evolutionary $N \times N$ -matrix, there are many efficient integrators for such systems, cf. [22]. In the present work, we are mainly interested in values of $s \leq \frac{1}{2}$, and thus *small to moderate stiffness*, which makes it possible to employ the classical *explicit fourth order Runge-Kutta method* (RK4). The latter is three to four times faster than the implicit code (IRK4) used in our previous work [25] and yet, all results obtained in the present paper agree with the ones in [25] up to errors of order 10^{-3} , or better.

The accuracy of the time-integration is controlled via the conservation of the numerically computed energy (1.3) and mass (1.2). Due to unavoidable numerical errors, the numerical energy $E_{\text{num}}(t) \equiv E((\mathcal{F}^{-1}\hat{u})(t, \cdot))$ will depend on time. In our simulations, the computed relative energy of the solution

$$(2.5) \quad \Delta_E = \left| \frac{E_{\text{num}}(t)}{E_{\text{num}}(0)} - 1 \right|$$

remains of the order 10^{-7} at worst, while the mass $M_{\text{num}}(t)$ is conserved up to errors of order 10^{-10} . In addition, we redo all of our critical numerical experiments using double the numerical resolution in the second run and confirming that the results agree within the desired accuracy of order 10^{-3} . Comparison of our RK4 scheme with other fourth-order methods reaffirm this accuracy (see the discussion in the appendix).

Remark 2.3. In [22] it was argued that the computed energy conservation overestimates the accuracy of the numerical solution by one to two orders of magnitude.

2.3. Singularity tracing in the complex plane. An advantage of Fourier methods is that they allow us to trace singularities in the complex plane via the asymptotic behavior of the Fourier transform. This was first used in a numerical context by Sulem et al. in [35] and has later been successfully applied in [23, 24].

Assume that $u(\cdot, x)$ can be analytically extended to a function $u(\cdot, z)$ within a strip around the real axis inside the complex plane. Suppose further that at a certain time $t \in \mathbb{R}$ this extended function u has a single essential singularity at $z_0(t) \in \mathbb{C}$, such that

$$u(t, z) \sim (z - z_0(t))^{\mu(t)} \quad \text{for } z \sim z_0(t), \text{ with } \mu(t) \notin \mathbb{N}.$$

Classical results in asymptotic analysis (see, e.g, [8]) then imply that the Fourier transform has the following asymptotic behavior, as $|\xi| \rightarrow \infty$:

$$(2.6) \quad |\hat{u}(t, \xi)| \sim \frac{1}{|\xi|^{1+\mu(t)}} e^{-\delta(t)|\xi|}, \quad \text{where } \delta(t) = \text{Im } z_0(t).$$

In [23, 24] the behavior of the FFT coefficients $\xi = k \in \frac{1}{2L}\mathbb{Z}$ within the numerical solution $u(t, \cdot)$ (which asymptotically should be of the form (2.6)) was used to quantitatively identify the time $t = t_f$ where the singularity $z_0(t) = x_0(t) + i\delta(t)$ hits the real axis, i.e., where $\delta(t_f) = 0$ and $u(t_f, x_0)$ becomes singular. The quantity $\delta \equiv \delta(t_f)$ is thereby identified by fitting the logarithm of the modulus of the FFT coefficients via linear regression. Since $|\xi|^{\mu+1}$ is only a logarithmic correction to the exponential behavior in (2.6), the quantity $\mu \equiv \mu(t_f) \in \mathbb{R}$ which characterizes the type of the singularity, is unfortunately less reliably determined than δ . However, in the case of the defocusing NLS, it was successfully used to detect the well-known cusp singularity $\mu = \frac{1}{3}$ in semiclassical limits, cf. [24].

In practice, the minimal resolved distance via Fourier methods is given by

$$m := 2\pi \frac{L}{N} \ll 1,$$

with $N \in \mathbb{N}$ being the number of FFT coefficients. This means that once $\delta(t) \leq m$, it is compatible to zero with numerical accuracy $\delta \simeq 0$. It was shown in [24] that the best results are obtained when the numerical code is stopped at a final time $t = t_f$ at which $\delta(t)$ actually vanishes, and this is the criterion to be applied also in the present paper. In our numerical simulations, we always find $0 < t_f \leq 20$.

Remark 2.4. Note that the expression (2.6) only holds in the presence of a single such singularity. If there are several singularities $z_j(t) \in \mathbb{C}$, $j = 1, \dots, J$, each of them contributes asymptotically, resulting in

$$\hat{u}(t, z) \sim \sum_{j=1}^J \frac{e^{z_j(t)|\xi|}}{|\xi|^{1+\mu_j(t)}}, \quad \text{as } |\xi| \rightarrow \infty.$$

This leads to interferences due to the presence of oscillations whenever $\text{Re } z_j \neq 0$. In such cases the vanishing of the first parameter δ_j will still indicate that a singularity has hit the real axis, but it will be difficult to identify the corresponding μ_j .

3. LINEAR FRACTIONAL SCHRÖDINGER EQUATION

In this section we shall study the linear case, i.e.,

$$(3.1) \quad i\varepsilon \partial_t u = (-\varepsilon^2 \Delta)^s u, \quad u|_{t=0} = v,$$

in order to gain some basic insight on the influence of the fractional dispersion within the time evolution. The solution to (3.1) is given by

$$(3.2) \quad u(t, x) = \mathcal{F}^{-1} \left(\widehat{v}(\xi) e^{-i\varepsilon^{2s-1} |\xi|^{2s} t} \right).$$

No time integration scheme is needed in this case; the inverse Fourier transform of (3.2) is just approximated for any given time t by an inverse FFT. For $\varepsilon = 0.1$, we will do so, by using $N = 2^{14}$ FFT modes for $x \in [-10\pi, 10\pi]$. As initial data we consider here

$$(3.3) \quad v(x) = \operatorname{sech}(x),$$

but the pictures remain qualitatively similar for other choices of v (such as those given in Section 4 below).

First, we compare the solution to the classical Schrödinger equation with $s = 1$ to the case with a slightly smaller fractional power $s = 0.8$. In Fig. 1, the modulus $|u|$ of both solutions is shown as a function of t and x . On the left, where $s = 1$, the initial hump is seen to be slowly dispersed as t becomes large. On the right, it can be seen that this effect is enhanced for $s = 0.8$.

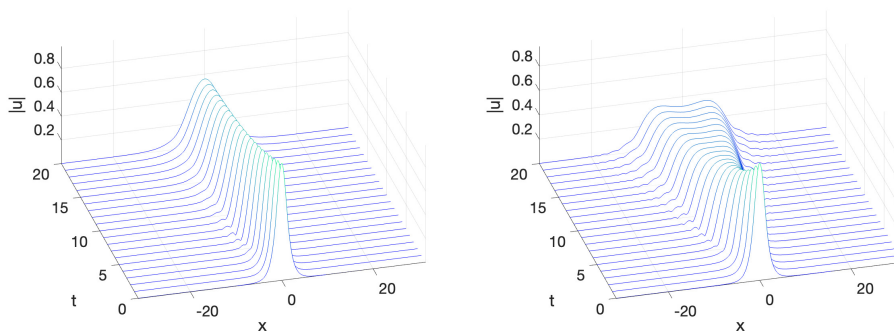


FIGURE 1. Solution to the linear equation (3.1) with $\varepsilon = 0.1$ and initial data (3.3): on the left for $s = 1$, on the right for $s = 0.8$.

For smaller values of $s \in (0, 1]$ it can be observed that the initial hump splits into two humps traveling towards $x \rightarrow \pm\infty$. In Fig. 2, we show the case $s = \frac{1}{2}$ and $s = 0.4$, respectively. The former corresponds to a *hyperbolic* Schrödinger equation with dispersion relation $\lambda(\xi) = |\xi|$, i.e.

$$(3.4) \quad i\partial_t u = \sqrt{-\Delta} u, \quad u|_{t=0} = v.$$

Note that in this case, the small semiclassical parameter ε cancels out of the equation, while for $s < \frac{1}{2}$ the power of ε appearing in formula (3.2) becomes negative. For $s = 0.4$ the solution for $t > 1$ appears to be almost separated into two humps with rather steep interior fronts (cf. the right picture in Fig. 2). Since the equation is linear, the solution nevertheless stays smooth at all times.

For even smaller values of the dispersion, the solution still develops two main humps, but the latter now decompose into several smaller crests. In Fig. 3, we show on the left the case with $s = \frac{1}{4}$, which corresponds to the energy critical regime

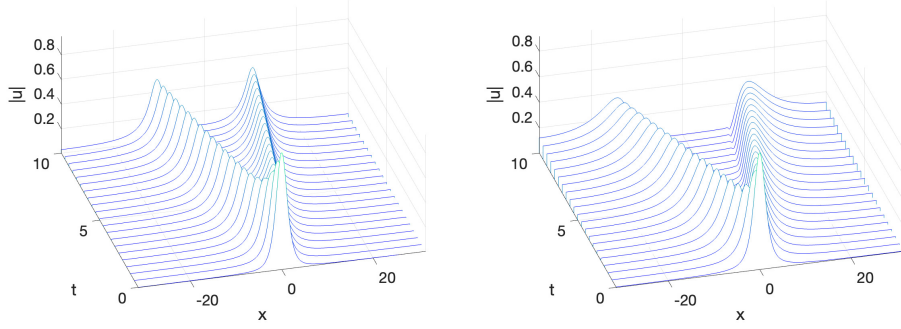


FIGURE 2. Solution to the linear equation (3.1) with $\varepsilon = 0.1$ and initial data (3.3): on the left for $s = \frac{1}{2}$, on the right for $s = 0.4$.

for the corresponding nonlinear model (2.1) with $p = 1$. On the right of the same figure we show the case with $s = \frac{1}{5}$. In this particular situation, the dispersion appears to lead to more than the two humps since there is a more agitated wave pattern to be observed, in particular at the interior boundary of the humps.

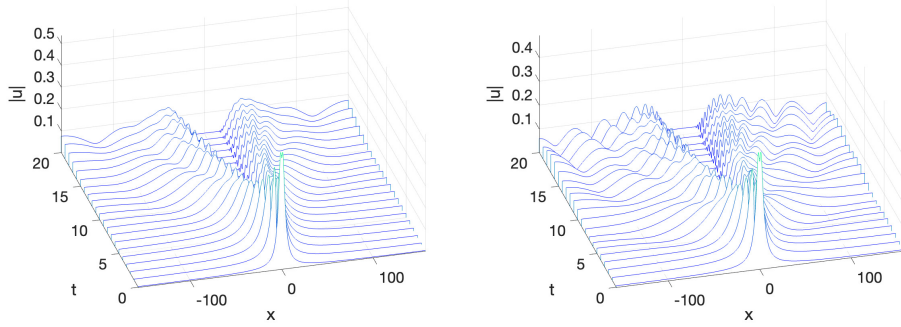


FIGURE 3. Solution to the linear equation (3.1) with $\varepsilon = 0.1$ and initial data (3.3): on the left for $s = \frac{1}{4}$, on the right for $s = \frac{1}{5}$.

These pictures can be partly explained by the fact that we expect the bulk of the particle density $\rho(t, x) = |u(t, x)|^2 \sim |a(t, x)|^2$ to approximately travel along the rays obtained via geometric optics, i.e.

$$x \mapsto X(t; x) = x + t\nabla\lambda(\xi)$$

The slope of these rays is given by the group velocity $v(\xi) = \nabla\lambda(\xi)$, which in $d = 1$ is equal to

$$v(\xi) = 2s \operatorname{sgn}(\xi) |\xi|^{2s-1}.$$

In particular, in the case of the hyperbolic equation (3.4) with $s = \frac{1}{2}$, the group velocity is $v(\xi) = \operatorname{sgn}(\xi) = \pm 1$, which explains the splitting of the initial hump in Fig. 2. For $s > \frac{1}{2}$ the solution is seen to interpolate between these two main directions of propagation in a smooth way. For $s < \frac{1}{2}$, however, the group velocity becomes singular at the origin. In this regime the effect of dispersion is “inverted” and wave packets with frequencies $|\xi| < 1$ will move faster than those with frequencies $|\xi| > 1$. We therefore expect a type of compression effect within the solution, as the slow frequencies within u try to “overtake” the high frequencies.

4. SOLUTION OF THE FRACTIONAL NLS: THE (SUB-)CRITICAL REGIME

In this section we shall expand on some of the numerical experiments from [25] and consider specifically the fNLS with cubic nonlinearity ($p = 1$), i.e.

$$(4.1) \quad i\varepsilon\partial_t u = (-\varepsilon^2\Delta)^s u + |u|^2 u, \quad u|_{t=0} = v,$$

for which we shall study the behavior of its solution in energy subcritical and critical cases. For $s = 1$ and $\varepsilon \ll 1$ this corresponds to the well known semiclassical limiting regime for cubic nonlinear Schrödinger equations, a particular case of the small dispersion limits studied in [14].

4.1. The subcritical regime. We first consider the subcritical regime with $s > \frac{1}{2}$, for which we use $N = 2^{14}$ FFT modes to resolve $x \in [-10\pi, 10\pi]$, and integrate equation (2.1) using $N_t = 10^3$ time steps. For the initial data v we shall consider three particular cases of smooth and rapidly decreasing functions. Namely,

$$(4.2) \quad (a) v(x) = \operatorname{sech}(x) \quad (b) v(x) = e^{-x^2} \quad (c) v(x) = e^{-x^4}.$$

In the left picture of Fig. 4, we show the modulus of the solution u to the semiclassically scaled NLS ($s = 1$) with $\varepsilon = 0.1$ and initial data (4.2)(a) as a function of t and x .

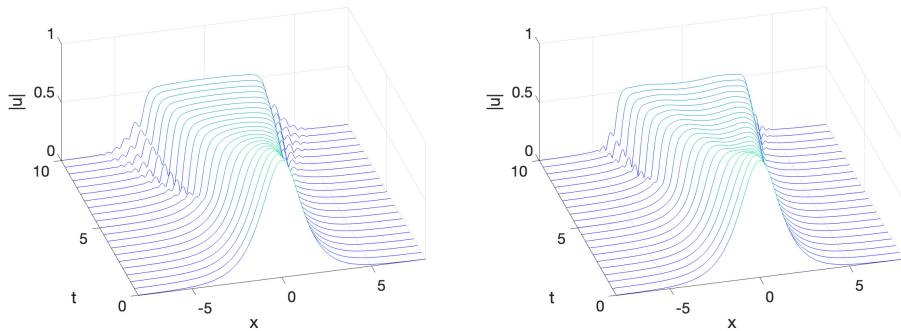


FIGURE 4. Solution to the cubic fNLS (4.1) with $\varepsilon = 0.1$ and initial data (4.2)(a): on the left for $s = 1$, on the right for $s = 0.8$.

As in the linear case, the dispersion leads to a broadening of the initial profile, but the nonlinearity implies a steepening of the gradients at the outer fronts. The small dispersion coefficient $\varepsilon = 0.1$ leads to oscillations near these fronts. As can be seen on the right of the same figure, the situation for $s = 0.8$ is qualitatively similar. In both of these cases, the general behavior can be interpreted as a combination of the linear dynamics (cf. Fig. 1) with additional small oscillations in the region of strong gradients.

4.2. The energy critical regime: emergence of turbulence. For computing the solution in the energy critical case $s = \frac{1}{4}$, we use $N = 2^{19}$ FFT modes for $x \in [-20\pi, 20\pi]$ and $N_t = 10^5$ time steps.

In Fig. 5 the modulus of the solution with initial data (4.2)(a) is shown as a function of t and x . It can be seen that $|u|$ exhibits rapid oscillations in between some very thin peaks. This behavior is consistent with the onset of a phenomenon called *weak turbulence*, i.e. a low-to-high frequency cascade within $\hat{u}(t, \xi)$, in which the mass $M(u)$ and energy $E(u)$ remain conserved, but $\hat{u}(t, \xi)$ shifts to increasingly higher values in $|\xi|$, or equivalently, to finer spatial scales in x , as $t \rightarrow +\infty$.

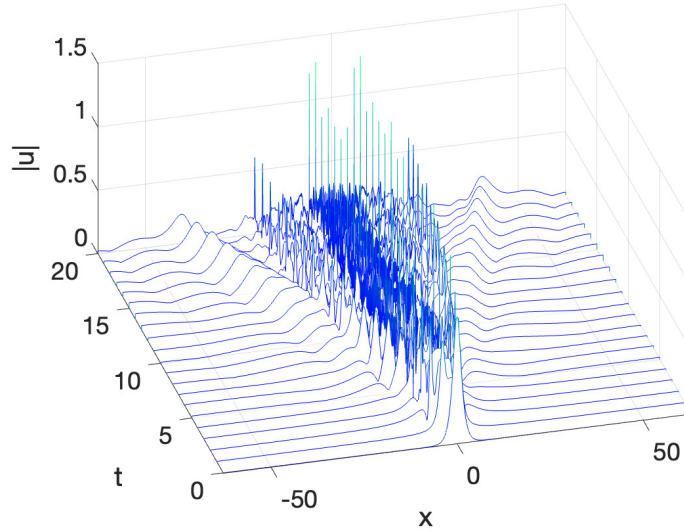


FIGURE 5. Solution to the energy-critical cubic fNLS (4.1) with $s = \frac{1}{4}$, $\varepsilon = 0.1$, and initial data (4.2)(a).

Remark 4.1. For cubically nonlinear Schrödinger equations ($s = 1$), the regime of weak turbulence has been rigorously studied in recent years, cf. [5, 11, 16, 29] and the references therein. In accordance with these studies, turbulent solutions u are to exhibit supercritical H^s -norms growth as $t \rightarrow \infty$, cf. Fig 8 and 9 below.

A plot of the (modulus of the) solution of Fig. 5 at time $t = 20$ is given in Fig. 6. It shows two large narrow peaks with finite amplitude and a zone of rapid oscillations in between. On the right of the same figure, a close-up of one of the peaks is shown, confirming that the solution is still well resolved numerically. We can see that the solution is still regular at this time. In particular, the oscillations do not increase their frequency near the peak.

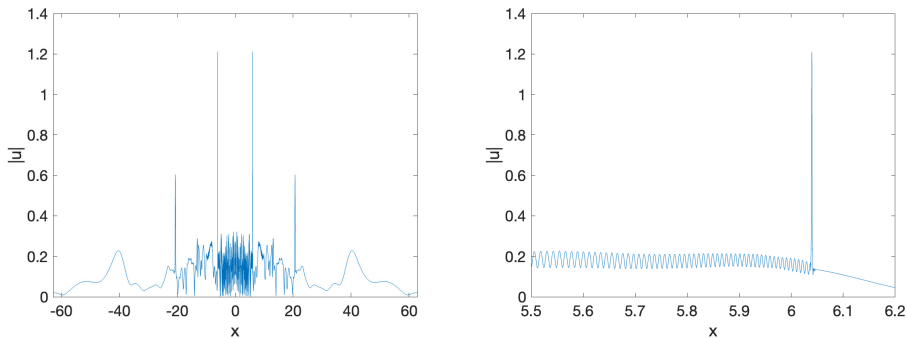


FIGURE 6. Left: Solution to the cubic fNLS (4.1) with $s = \frac{1}{4}$, $\varepsilon = 0.1$, and initial data (4.2)(a) at $t = 20$. Right: a close-up near one of the peaks.

The regularity of u is confirmed by the fact that the FFT coefficients of $\hat{u}(t, k)$ at $t = 20$ span about five orders of magnitude, cf. the left of Fig. 7. The fitting

parameter $\delta(t)$, appearing in the asymptotic formula (2.6), is shown as a function of time on the right of the same figure. We see that $\delta(t)$ is clearly decreasing, indicating that an essential singularity within $u(t, z)$ approaches the real axis. However, at $t = 20$ the parameter $\delta > m$ and hence, still above the minimal distance m resolved by the FFT discretization.

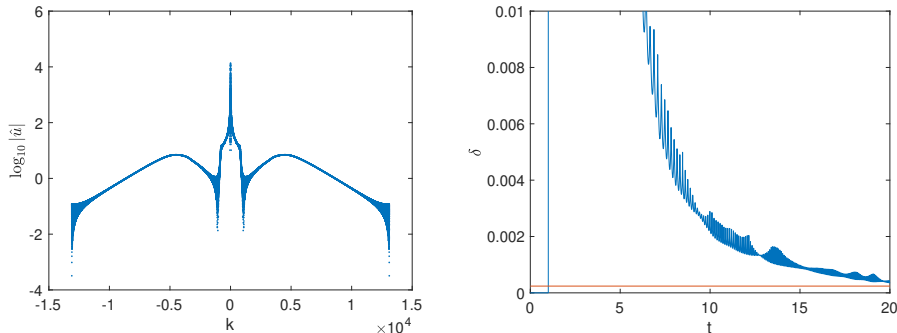


FIGURE 7. Left: FFT coefficients of the solution from Figure 6. Right: the fitting parameter δ as a function of time.

Remark 4.2. Numerically it cannot be excluded that $\delta(t)$ will eventually drop below the threshold m at a much later time $t \gg 20$. In order to reach such time-scales, a much higher resolution in both x and t will be needed, which is beyond the scope of the current paper.

Further qualitative properties of the solution are shown in the next set of figures: In Fig. 8 on the left, we show the L^∞ -norm of $u(t, \cdot)$ as a function of time. It is

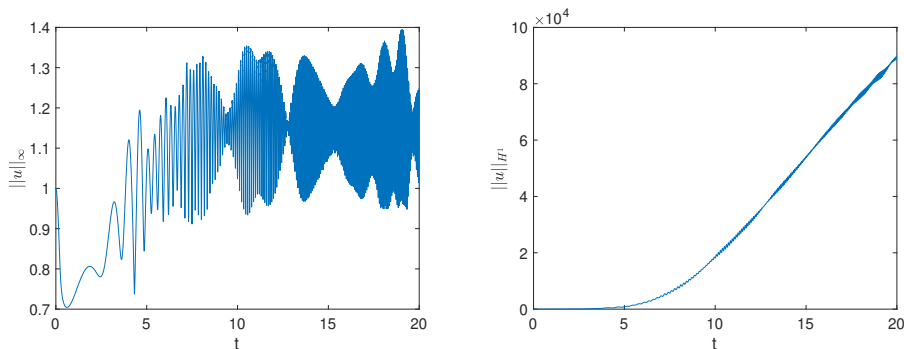


FIGURE 8. The L^∞ -norm and the \dot{H}^1 -norm of the solution to the cubic fNLS (4.1) with $s = \frac{1}{4}$, $\varepsilon = 0.1$, and initial data (4.2)(a).

seen to be highly oscillatory, which is due to the oscillatory behavior of the solution and the fact that we numerically determine the values of $\|u(t, \cdot)\|_{L^\infty}$ only on grid points (the actual maximum of the solution might not be located on a point of the numerical grid). Extrapolating from the time interval shown, we expect the L^∞ -norm to remain bounded in time. The \dot{H}^1 -norm of u , shown on the right of Fig. 8, is clearly growing in t but seems to have an inflection point around $t \approx 20$. Thus we do not expect the appearance of a finite time singularity in this case.

This belief is strengthened by the time-decay of higher order L^q -norms of $u(t, \cdot)$ with $q > 2$. Shown on the left of Fig. 9 is the case with $q = 8$. In addition, we also plot the Sobolev-critical $\dot{H}^{1/2}$ -norm of u on the right of the same figure. After initially growing in t , it appears to become saturated and thus bounded.

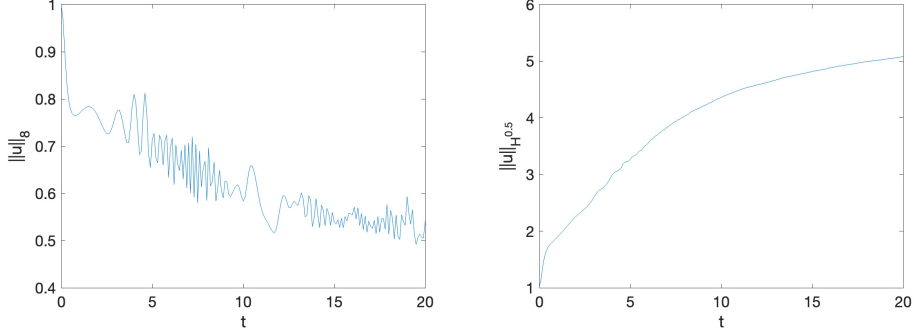


FIGURE 9. The L^8 -norm and the $\dot{H}^{1/2}$ -norm of the solution to the cubic fNLS (4.1) with $s = \frac{1}{4}$, $\varepsilon = 0.1$, and initial data (4.2)(a), both norms normalized to 1 for $t = 0$.

To ensure that these findings are indeed reliable we redo our simulation: using varying time-steps, we first find that for our RK4 scheme the L^∞ -norm of the difference between the numerical solution obtained with $N_t = 5 \cdot 10^5$ and the one with $N_t = 10^5$ is of the order $2.4 \cdot 10^{-4}$, whereas the difference to the case with $N_t = 5 \cdot 10^4$ is of the order $6.7 \cdot 10^{-3}$. Thus for fixed spatial resolution, the numerical error due to the time discretization decreases as expected with N_t . In a similar way we can study the effect of spatial resolution. For fixed $N_t = 10^5$, the difference between the numerical solution with $N = 2^{19}$ and $N = 2^{20}$ Fourier modes can be seen on the left of Fig. 10. The FFT coefficients for the latter case at the final time are given on the right of the same figure. Visibly they decrease exponentially, confirming the regularity of the solution. In the appendix, we also compare our results with those obtained by two other numerical schemes to find that they agree within an L^∞ -difference of order 10^{-4} .

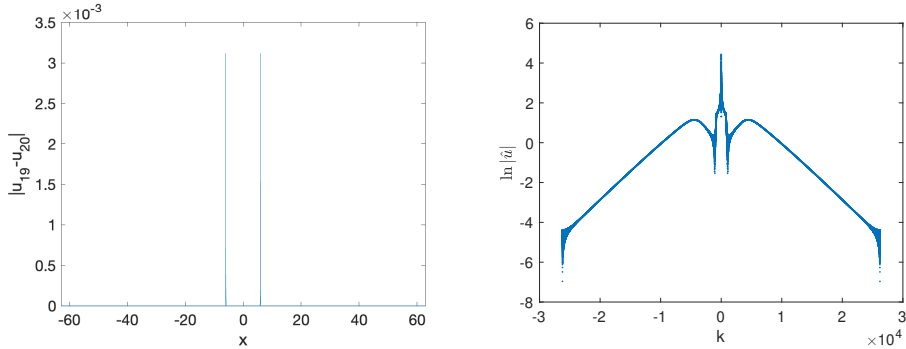


FIGURE 10. Left: difference between the numerical solution in Fig. 6 for $N = 2^{19}$ and $N = 2^{20}$ FFT modes. Right: FFT coefficients of the solution from Fig. 6 with $N = 2^{20}$.

4.3. Further examples in the critical regime. The situation remains qualitatively similar in the case of Gaussian initial data (4.2)(b). The corresponding modulus of the solution u at time $t = 20$ is shown on the left of Fig. 11. Notably

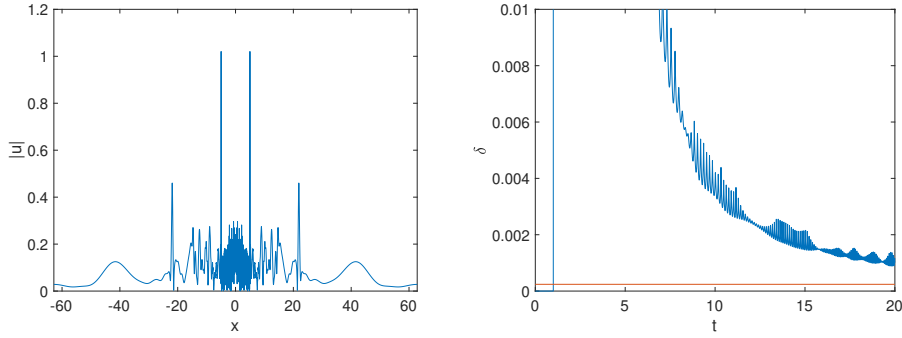


FIGURE 11. Left: solution to the cubic fNLS (4.1) with $s = \frac{1}{4}$, $\varepsilon = 0.1$, and initial data (4.2)(b) at $t = 20$. Right: the fitting parameter δ as a function of time.

the bulk of $|u|$ is more localized than in the previous case. The function $\delta(t)$ is shown on the right hand side of the same figure. As one can see, $\delta(t)$ decays slower than in the previous case and remains clearly above the threshold m .

For the even faster decaying (super Gaussian) initial data (4.2)(c), the solution at the time $t = 10$ is shown on the left of Fig. 12. There are again rapid oscillations

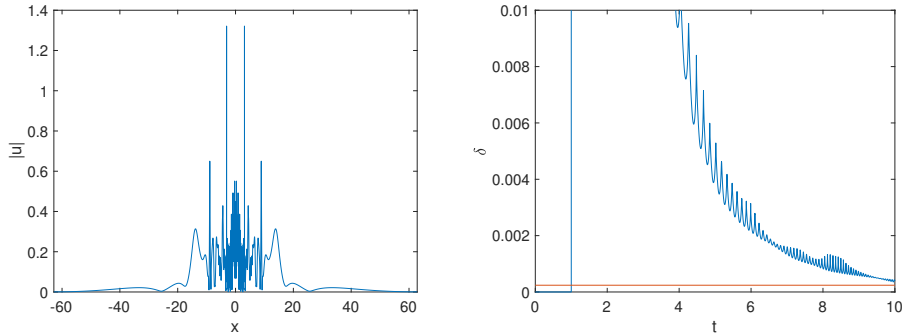


FIGURE 12. Left: solution to the cubic fNLS (4.1) with $s = \frac{1}{4}$, $\varepsilon = 0.1$, and initial data (4.2)(c) at $t = 10$. Right: the fitting parameter δ as a function of time.

located between two clearly visible sharp peaks, but the solution is even more localized than before. In addition, the parameter $\delta(t)$ decreases more rapidly than in the previous two cases.

5. SOLUTION OF THE FRACTIONAL NLS: THE SUPERCRITICAL REGIME

5.1. Cubic nonlinearity. We now turn to the supercritical regime, and first consider the following fNLS with cubic nonlinearity:

$$(5.1) \quad i\varepsilon \partial_t u = (-\varepsilon^2 \Delta)^{1/5} u + |u|^2 u, \quad u|_{t=0} = v.$$

Recall that for cubic nonlinearities the energy critical power is $s_* = \frac{1}{4}$, hence choosing $s = \frac{1}{5}$ puts us firmly in an energy supercritical regime. As initial data we shall again choose one of the functions given in (4.2).

First, in the case where $v = \text{sech}(x)$, the resulting (weakly turbulent) time-evolution of $|u|$ is shown in the next figure.

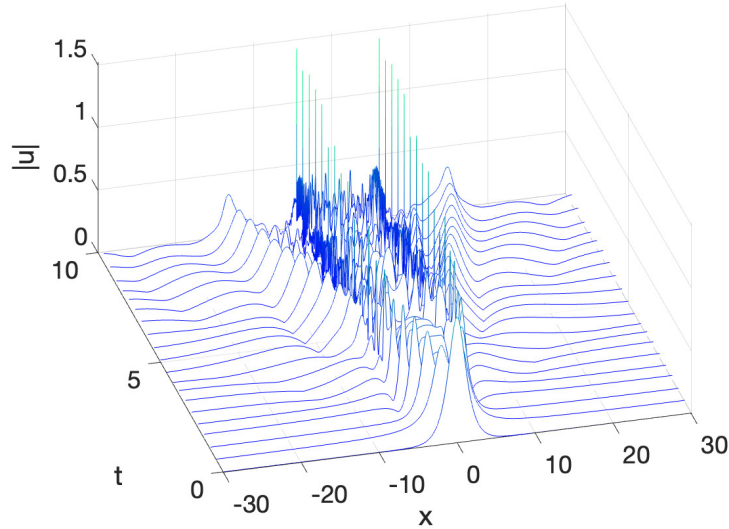


FIGURE 13. Solution to the cubic fNLS (5.1) with $\varepsilon = 0.1$, $s = \frac{1}{5}$ and initial data (4.2)(a).

In this case, the numerical value of $\delta(t)$ vanishes at time $t_f = 9.8$. The code is stopped at this point, and the solution at the final time can be seen in Fig. 14.

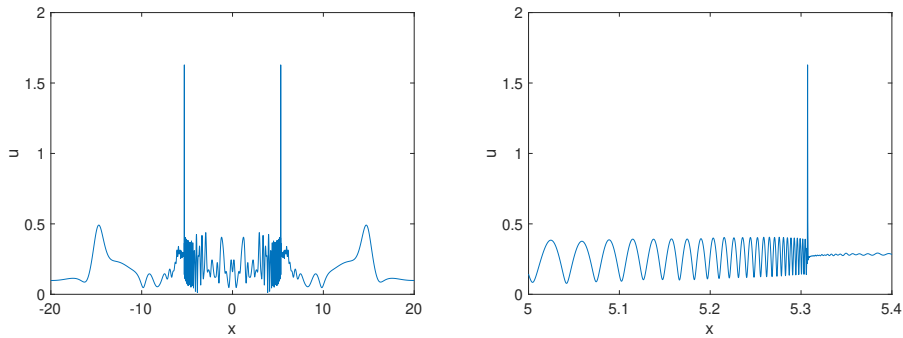


FIGURE 14. Left: solution to the cubic fNLS (5.1) with $\varepsilon = 0.1$, $s = \frac{1}{5}$ and initial data (4.2)(a) at the final time $t_f = 9.8$. Right: a close-up near one of the peaks.

As in the energy critical case there appear to be strong peaks at the left and right front of the two humps with rapid oscillations in between. However, in contrast to the previous (sub-)critical situation, these oscillations become more and more “compressed” close to the peaks. This is clearly visible on the right of the same figure, which shows a close-up of the singular region around $x \simeq 5.31$.

The fitting of the FFT coefficients according to (2.6) yields a value of $\mu \simeq -\frac{1}{3}$ (numerically, we obtain $\mu = -0.327\dots$). This indicates a blow-up of the L^∞ -norm of u , since, according to the theory presented in Section 2.3, we expect

$$|u(t_f, x)| \sim |x - x_0|^{-\frac{1}{3}} \text{ where } x_0 \simeq \pm 5.31.$$

However, one might need to take this with a grain of salt (cf. the discussion at the end of Section 2.3). A finite amplitude $|u(t_f, x_0)|$ which exhibits blow-up within some higher order L^q -norm with $q > 2$, or some higher order H^s -norm with $s > \frac{1}{2}$, seems equally likely, and hard to decide numerically. One should also note that the relatively small value of $|\mu| \simeq \frac{1}{3}$ implies that the singularity at x_0 would yield a (very) large L^∞ -norm only if x_0 were by chance *exactly* on one of the grid points.

The FFT coefficients within \hat{u} at time $t_f = 9.8$ are shown on the left of Fig. 15. On the right of the same figure we also show the L^∞ -norm of the solution u as a function of time. It can be seen that $\|u(t, \cdot)\|_{L^\infty}$ is slowly growing in time and again highly oscillatory.

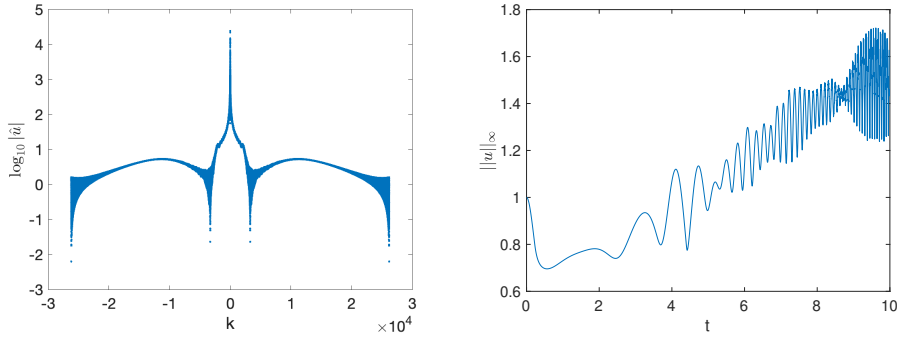


FIGURE 15. Left: FFT coefficients of the solution from Figure 14. Right: the L^∞ -norm of u as a function of time.

In Fig. 16 we show the behavior of the (energy-controlled) \dot{H}^s -norm of u and of the supercritical \dot{H}^1 -norm, both as functions of time.

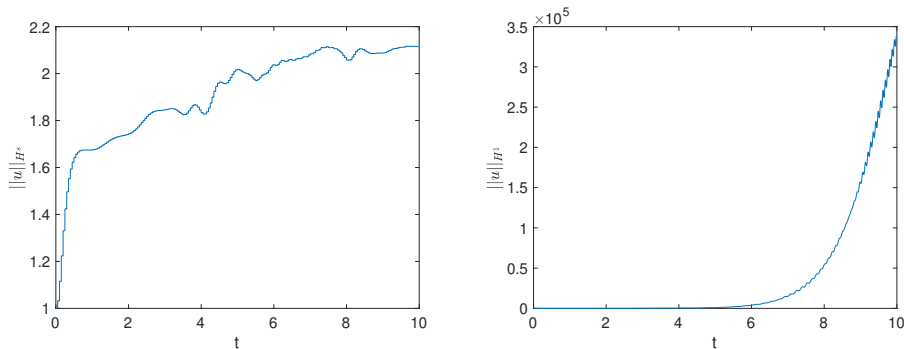


FIGURE 16. The \dot{H}^s -norm (left) and the \dot{H}^1 -norm (right) of the solution to the cubic fNLS (5.1) with $\varepsilon = 0.1$, $s = \frac{1}{5}$ and initial data (4.2)(a).

It can be seen that the former remains bounded, due to (numerically almost) energy conservation, whereas the latter is clearly rapidly growing, indicating a

finite-time blow-up. Other supercritical Sobolev norms H^s with $s \geq 1$ (not shown here) behave similarly. In contrast, all L^q -norms of $u(t, \cdot)$ with $2 \leq q \leq 10$ remain bounded as functions of time, cf. Fig. 17 which shows the case for $q = 10$. On the right of the same figure we show the Sobolev critical $\dot{H}^{1/2}$ -norm, which is seen to be moderately growing.

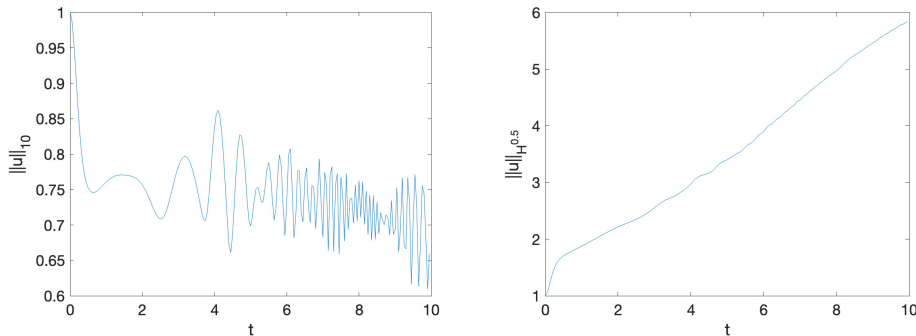


FIGURE 17. The L^{10} -norm (left) and the $\dot{H}^{1/2}$ -norm (right) of the solution to the cubic fNLS (5.1) with $\varepsilon = 0.1$, $s = \frac{1}{5}$ and initial data (4.2)(a), both normalized to 1 for $t = 0$.

Overall, the numerical pictures suggest the *formation of a small-scale coherent structure* associated with the transfer of energy to arbitrarily small spatial regions: a “spike” of large amplitude, whose width seems to go to zero, approaching a point discontinuity at some finite time $T \gtrsim t_f$. All of this is combined with a region of high frequency oscillations within u , suggesting the appearance of a singularity in *both* the amplitude $|u|$ and the phase $\varphi = \arg u$.

Remark 5.1. Very recently, numerical and analytical evidence for a similar phenomenon, called *-3/2-cascade*, has been found in the case of fully resonant Hamiltonian systems with cubic nonlinearity, cf. [1, 2]. The latter can be seen as a non-dispersive toy model, obtained from the fNLS by ignoring the fractional Laplacian and retaining only cubically resonant frequencies $k \in \mathbb{Z}$, which satisfy the relation: $|k_1|^{2s} - |k_2|^{2s} + |k_3|^{2s} = |k|^{2s}$ for $k_1 - k_2 + k_3 = k$. In particular, the figures in [1, 2] show the formation of a “spike”, which very much resembles our findings, minus the additional high frequency oscillations (which presumably are due to non-resonant frequencies).

5.2. Additional simulations in the supercritical cubic case. For Gaussian initial data (4.2)(b), the code is stopped at time $t_f = 9.59$, as $\delta = 0$ at this time. We thereby obtain a fitted value of $\mu \simeq -0.33 \dots$. The solution at the final recorded time is shown in Fig. 18. When compared to Fig. 14, the solution is qualitatively similar but notably more confined. A close-up of the solution near one of the peaks on the right of Fig. 18 again shows compression of the oscillations near the presumed singularity at $x_0 \simeq 3.76$. Finally, for super-Gaussian initial data (4.2)(c), we find that numerically $\delta = 0$ at time $t_f = 5.46$. The fitted value for μ is again compatible with $\mu \simeq -\frac{1}{3}$ (we obtain $\mu = -0.32 \dots$). The solution at the final time is shown in Fig. 19 on the left, with a close up near the presumed singularity on the right.

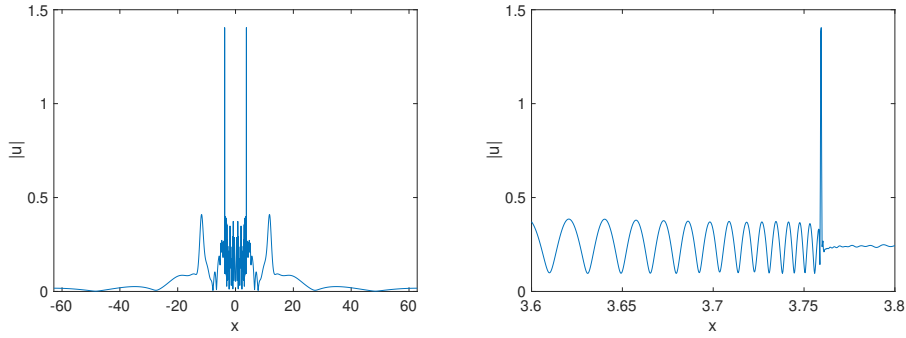


FIGURE 18. Left: solution to the cubic fNLS (5.1) with $\varepsilon = 0.1$, $s = \frac{1}{5}$ and initial data (4.2)(b) at the final time $t_f = 9.59$. Right: a close-up near one of the peaks.

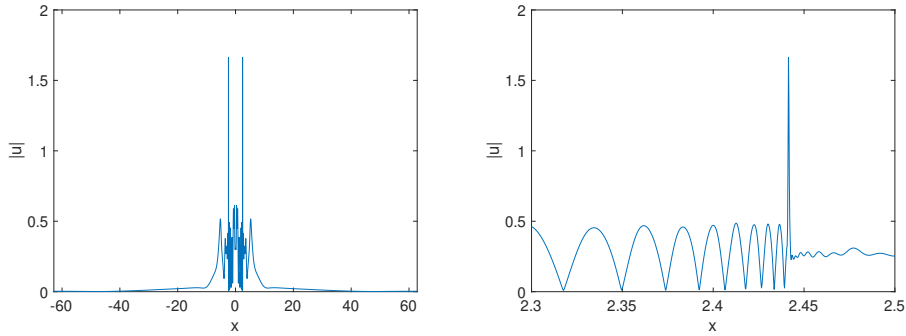


FIGURE 19. Left: solution to the cubic fNLS (5.1) with $\varepsilon = 0.1$, $s = \frac{1}{5}$ and initial data (4.2)(c) at the final time $t_f = 9.59$. Right: a close-up near one of the peaks.

The above runs have been repeated with $N = 2^{20}$ FFT modes, and all of our results agree within the estimated numerical accuracy. This adds more confirmation to the observation of a singularity in the energy supercritical case with cubic nonlinearity $p = 1$.

In addition, we can do numerical simulations for $p = 1$ and other supercritical choices of the fractional parameter $s < \frac{1}{4}$. Some results, using super-Gaussian initial data (4.2)(c), can be seen in the box below:

s	t_f	μ
0.2	5.46	-0.32
0.19	5.014	-0.31
0.15	3.9354	-0.29

The fact that in all of these cases the solution u behaves qualitatively similar, suggests that the singularity does *not* depend on a particular choice of the parameter $s < s_*$, at least in the cubic case $p = 1$.

Remark 5.2. One might suspect from our findings that the parameter $\mu \in \mathbb{R}$ goes to zero as $s \rightarrow 0$. This would be consistent with the fact that the limiting equation (2.3), formally obtained for $s = 0$, does not suffer from a singularity. However, we were not able to give conclusive numerical evidence for a (possible) dependence of μ on $s \in (0, 1]$.

5.3. Other nonlinearities. Finally, we shall try to answer the question whether the previous findings are sensitive to the choice of the nonlinear power $p \in \mathbb{N}$.

To this end, we first consider a quintic nonlinearity with $p = 2$. Here, the critical index is $s_* = \frac{1}{3}$, hence bigger than in the previous (cubic) case. More specifically, we shall study the supercritical time-evolution of

$$(5.2) \quad i\varepsilon \partial_t u = (-\varepsilon^2 \Delta)^{1/4} u + |u|^4 u, \quad u|_{t=0} = e^{-x^4}.$$

Numerically we find $\delta(t) = 0$ at time $t_f = 8.47$. The associated parameter $\mu = -0.38\dots$ and thus, again compatible with $\mu \simeq -\frac{1}{3}$. The solution at the final time is shown in Fig. 20. Overall, the quintic case behaves qualitatively similar to the one with a cubic nonlinearity. In particular, the oscillations again become strongly compressed near the presumed singularity at $x_0 \simeq \pm 4.1$.

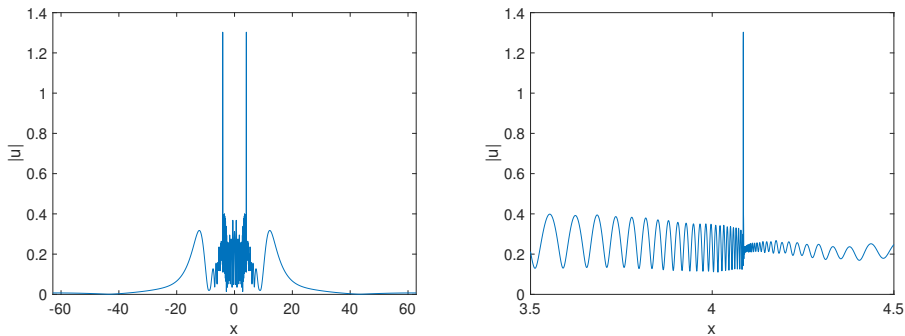


FIGURE 20. Left: solution to the quintic fNLS (5.2) with $\varepsilon = 0.1$ and $s = \frac{1}{4}$ at the final time $t_f = 8.47$. Right: a close-up near one of the peaks.

Surprisingly, the same super-Gaussian initial data do not seem to yield a singularity for even higher nonlinear powers $p \geq 3$. It can be seen on the left of Fig. 21 that no singularity appears for $p = 3$, even though the solution still displays a weakly turbulent behavior. Even more surprisingly, the right picture within Fig. 21 shows that for $p = 4$ the time-evolution yields a purely dispersive solution, similar to the linear case (compare with Fig. (3)).

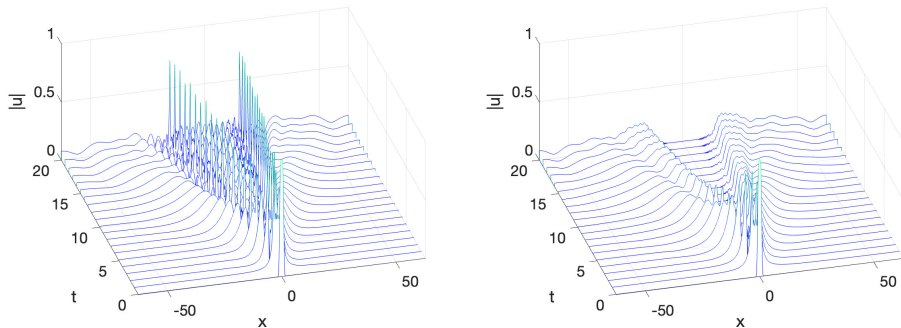


FIGURE 21. Solution to the fNLS equation (2.1) with $\varepsilon = 0.1$, $s = \frac{1}{4}$ and initial data (4.2)(c): on the left for nonlinear power $p = 3$ and on the right for $p = 4$.

However, once we chose bigger initial data, such as

$$(5.3) \quad u|_{t=0}(x) = 2e^{-x^2},$$

a singular behavior again reemerges. Indeed, we find that in this case the code stops already at $t_f = 1$, to yield a fitted $\mu \simeq -0.31$. The solution at the final time is shown on the left of Fig. 22. A close-up near one of the peaks (shown at the right of the same figure) indicates a compression of the phase similarly to our previous supercritical cases.

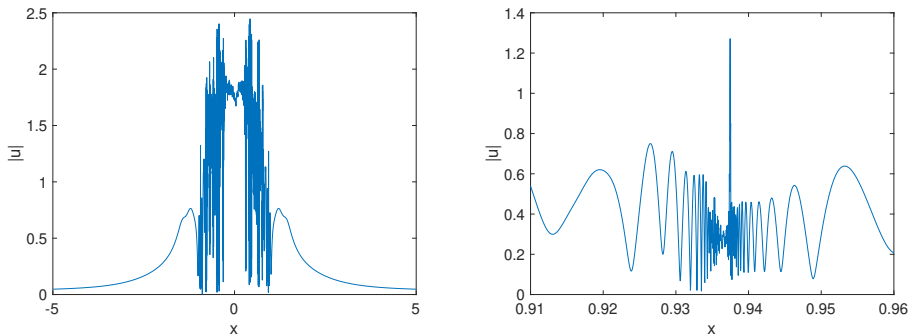


FIGURE 22. Left: Solution to the fNLS equation (2.1) with $\varepsilon = 0.1$, $s = \frac{1}{4}$, $p = 3$, and initial data (5.3) at the final time $t_f = 1$. Right: a close-up of the solution near one of the peaks.

These findings suggest that such highly oscillatory singularities can only be observed for initial data with sufficiently large L^q -norms. It is beyond the scope of the current article to quantify the associated threshold and its precise dependence on the nonlinear power $p \in \mathbb{N}$. At this point, it is also unclear if the highly oscillatory dynamics produced in our numerical simulations is of the same type as the blow-up described in [33]. Since our results strongly depend on the choice of $s < s_*$, it could be that our (presumed) singularities are of a different nature than the ones found in [33]. As far as we know, however, there have not yet been any successful numerical simulations of the singularity formation proved in [33].

APPENDIX A. COMPARISON WITH OTHER NUMERICAL METHODS

The convergence of the numerical scheme (RK4) used in the present work was discussed in detail in [22] for the case of the classical nonlinear Schrödinger equation ($s = 1$). In the following we briefly compare and contrast (RK4) with some other numerical approaches one might want to pursue:

We first note that the exponential integrators discussed in [22] can in principle also be applied in the present case, but with the following caveats: the exponential integrator appearing in our case is of the form

$$S(h) = e^{-i\varepsilon^{2s-1}|k|^{2s}h},$$

where the time-step is $\Delta t = h > 0$. Multiplying the numerical solution by such a factor becomes problematic whenever $\varepsilon^{2s-1}|k|^{2s}h = 0 \pmod{2\pi}$, which implies the CFL-type condition $h < 2\pi/(\varepsilon^{2s-1}|k|^{2s})$. On the one hand, this condition can enforce time steps that effectively become too small in our case which requires sufficiently high resolution (in Fourier space). On the other hand, Driscoll's [12]

composite Runge-Kutta method can suffer from instabilities for larger time steps which enforces less efficient implementations, see, e.g. the discussion in [15].

The most efficient method from those discussed in [22] are fourth order splitting schemes, originally described in [37]. Below, we show a comparison of our (explicit) RK4 algorithm with such a fourth order splitting scheme, as well as with an implicit Runge-Kutta method (IRK4). We thereby focus on the example given in Fig. 6, i.e. the fNLS with cubic nonlinearity ($p = 1$) in the energy-critical case ($s = \frac{1}{4}$). We again chose $\varepsilon = 0.1$ and initial data $v(x) = \operatorname{sech}(x)$. In Fig. 23 we show the difference in L^∞ -norm between our results and the other two aforementioned methods. We thereby use the same numerical parameters N and N_t for all three methods, ensuring numerical errors smaller than 10^{-3} . As expected, the resulting difference is of the order of 10^{-4} , the biggest deviations appearing at the sharp peaks within the solution u .

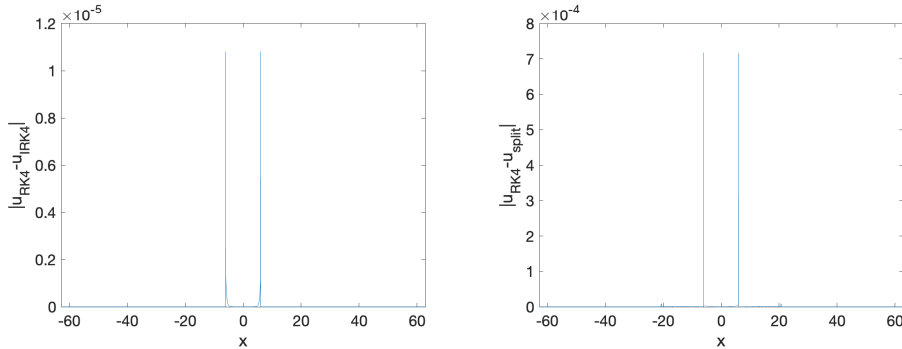


FIGURE 23. Left: Difference between the numerical solution of Figure 6 and a solution obtained using IRK4. Right: Difference between the numerical solution of Figure 6 and a fourth order splitting method.

We note that the splitting scheme is roughly 30% faster (Matlab timings) than our RK4. The reason why we only use it as reference solution in the present paper is that numerical resonances limit the achievable accuracy to the order $\mathcal{O}(10^{-8})$, cf. the discussion in [22].

REFERENCES

1. A. Biasi, Exact solutions for a coherent phenomenon of condensation in conservative Hamiltonian systems. *Phys. Rev. E* **110** (2024), no. 3, 034107, 14 pp.
2. A. Biasi and P. Gérard, Energy cascades and condensation via coherent dynamics in Hamiltonian systems. Preprint [arXiv:2412.03663](https://arxiv.org/abs/2412.03663).
3. T. Boulenger, D. Himmelsbach, and E. Lenzmann, Blowup for fractional NLS. *J. Funct. Anal.* **271** (2016), no. 9, 2569–2603.
4. J. Bourgain, Problems in Hamiltonian PDE'S. *Geom. Funct. Anal.* (2000), Special volume: Vision in Mathematics Part I, 32–56.
5. T. Buckmaster, P. Germain, Z. Hani, and J. Shatah, Onset of the wave turbulence description of the longtime behavior of the nonlinear Schrödinger equation. *Invent. math.* **225** (2021), 787–855.
6. G. Cao-Labora, J. Gómez-Serrano, J. Shi, and G. Staffilani, Non-radial implosion for the defocusing nonlinear Schrödinger equation in \mathbb{T}^d and \mathbb{R}^d . Preprint [arXiv:2410.04532](https://arxiv.org/abs/2410.04532).
7. R. Carles, *Semi-classical Analysis for Nonlinear Schrödinger Equations*, World Scientific, Hackensack, NJ, 2008.
8. G. Carrier and M. K. C. Pearson, *Functions of a Complex Variable, Theory and Technique*. Society for Industrial and Applied Mathematics (SIAM), Philadelphia, PA, 2005.

9. B. Choi and A. Aceves, Well-posedness of the mixed-fractional nonlinear Schrödinger equation on \mathbb{R}^2 . *Partial Differential Equ. Appl. Math.* **6** (2022), 100406, 11pp.
10. J. Colliander, G. Simpson, and C. Sulem, Numerical simulations of the energy supercritical nonlinear Schrödinger equation. *J. Hyperbolic Diff. Equ.* **7** (2010), no. 2, 279–296.
11. J. Colliander, M. Keel, G. Staffilani, H. Takaoka, and T. Tao, Weakly turbulent solutions for the cubic defocusing nonlinear Schrödinger equation. *Invent. Math.* **181** (2010), 39–113.
12. T.A. Driscoll, A composite Runge-Kutta method for the spectral solution of semilinear PDEs, *J. Comput. Phys.*, 182 (2002), pp. 357–367.
13. B. Dubrovin, T. Grava, and C. Klein, On universality of critical behavior in the focusing nonlinear Schrödinger equation, elliptic umbilic catastrophe and the tritonquée solution to the Painlevé-I equation. *J. Nonlinear Sci.* **19** (2009), no. 1, 57–94.
14. B. Dubrovin, T. Grava, C. Klein, and A. Moro, On critical behaviour in systems of Hamiltonian partial differential equations. *J. Nonlinear Sci.* **25** (2015), 631–707.
15. T. Grava, C. Klein and G. Pitton, *Numerical study of the Kadomtsev–Petviashvili equation and dispersive shock waves*, Proc. R. Soc. A 474: 20170458. <http://dx.doi.org/10.1098/rspa.2017.0458> (2018).
16. Z. Hani, Long-time instability and unbounded Sobolev orbits for some periodic nonlinear Schrödinger equations. *Arch. Ration. Mech. Anal.* **211** (2014), 929–964.
17. Y. Hong and Y. Sire, On Fractional Schrödinger Equations in Sobolev spaces. *Comm. Pure Appl. Anal.* **14** (2015), no. 6, 2265–2282.
18. M. Ifrim and D. Tataru, Global solutions for 1D cubic defocusing dispersive equations: Part I. *Forum Math. Pi* **11** (2023), paper no. e31, 1–46.
19. M. Ifrim and D. Tataru, Global solutions for 1D cubic defocusing dispersive equations, Part IV: general dispersion relations. Preprint [arXiv:2410.10052](https://arxiv.org/abs/2410.10052).
20. A. Ionescu and F. Pusateri, Nonlinear fractional Schrödinger equations in one dimension. *J. Funct. Anal.* **266** (2014), no. 1, 139–176.
21. K. Kirkpatrick, E. Lenzmann, and G. Staffilani, On the continuum limit for discrete NLS with long-range lattice interactions. *Comm. Math. Phys.* **317** (2013), 563–591.
22. C. Klein, Fourth order time-stepping for low dispersion Korteweg-de Vries and nonlinear Schrödinger equations. *Electronic Trans. Num. Anal.* **29** (2008), 116–135.
23. C. Klein and K. Roidot, Numerical study of shock formation in the dispersionless Kadomtsev–Petviashvili equation and dispersive regularizations. *Phys. D* **265** (2013), 1–25.
24. C. Klein and K. Roidot, Numerical study of the semiclassical limit of the Davey–Stewartson II equations. *Nonlinearity* **27** (2014), 2177–2195.
25. C. Klein, C. Sparber, and P. Markowich, Numerical study of fractional nonlinear Schrödinger equations. *Proc. R. Soc. Lond. Ser. A* **470** (2014), 20140364, 26pp.
26. C. Klein and N. Stoilov, Numerical methods for fractional PDEs. *Nonlinear Syst. Complex.* **37** (2024), 187–208.
27. C. Klein and N. Stoilov, Multi-domain spectral approach to rational order fractional derivatives. *Stud. Appl. Math.* **152** (2024), no. 4, 1110–1132.
28. J. Krieger, E. Lenzmann, and P. Raphaël, Nondispersive solutions to the L^2 -critical half-wave equation. *Arch. Ration. Mech. Anal.* **209** (2013), no. 1, 61–129.
29. S. Kuksin, Oscillations in space-periodic nonlinear Schrödinger equations. *Geom. Funct. Anal.* **7** (1997), no. 2, 338–363.
30. N. Laskin, Fractional quantum mechanics and Lévy path integrals. *Phys. Lett. A* **268** (2000), no. 4–6, 298–305.
31. F. Merle, P. Raphaël, I. Rodnianski, and J. Szeftel, On the implosion of a compressible fluid I: smooth self-similar inviscid profiles. *Ann. of Math.* **196** (2022), no. 2, 567–778.
32. F. Merle, P. Raphaël, I. Rodnianski, and J. Szeftel, On the implosion of a compressible fluid II: singularity formation. *Ann. of Math.* **196** (2022), no. 2, 779–889.
33. F. Merle, P. Raphaël, I. Rodnianski, and J. Szeftel, On blow up for the energy super critical defocusing nonlinear Schrödinger equations. *Invent. math.* **227** (2022), 247–413.
34. C. Sulem and P. L. Sulem, *The nonlinear Schrödinger equation: Self-Focusing and Wave Collapse*. Springer Series in Mathematical Sciences vol. 139, Springer Verlag, 1999.
35. C. Sulem, P.-L. Sulem, and H. Frisch, Tracing complex singularities with spectral methods. *J. Comput. Phys.* **50** (1983), no. 1, 138–161,
36. L. Trefethen. *Spectral Methods in Matlab*. Society for Industrial and Applied Mathematics (SIAM), Philadelphia, PA, 2000.
37. H. Yoshida, Construction of higher order symplectic integrators, *Phys. Lett. A*, 150 (1990), pp. 262–268.

(C. Klein) INSTITUT DE MATHÉMATIQUES DE BOURGOGNE, UNIVERSITÉ DE BOURGOGNE-EUROPE,
INSTITUT UNIVERSITAIRE DE FRANCE, 9 AVENUE ALAIN SAVARY, BP 47870, 21078 DIJON CEDEX
Email address: `christian.klein@u-bourgogne.fr`

(C. Sparber) DEPARTMENT OF MATHEMATICS, STATISTICS, AND COMPUTER SCIENCE, M/C 249,
UNIVERSITY OF ILLINOIS AT CHICAGO, 851 S. MORGAN STREET, CHICAGO, IL 60607, USA
Email address: `sparber@uic.edu`